INTERNATIONAL JOURNAL FOR NUMERICAL METHODS IN FLUIDS
Int. J. Numer. Meth. Fluids 2007; **53**:1727–1754
Published online 10 October 2006 in Wiley InterScience (www.interscience.wiley.com). DOI: 10.1002/fld.1381

A hybrid immersed-boundary and multi-block lattice Boltzmann method for simulating fluid and moving-boundaries interactions

Yi Sui[1], Yong-Tian Chew[1], Partha Roy[2] and Hong-Tong Low[2,*,†]

[1]*Department of Mechanical Engineering, National University of Singapore, 9 Engineering Drive 1, Singapore 117576, Singapore*
[2]*Division of Bioengineering, National University of Singapore, 9 Engineering Drive 1, Singapore 117576, Singapore*

SUMMARY

A numerical method is developed for modelling the interactions between incompressible viscous fluid and moving boundaries. The principle of this method is introducing the immersed-boundary concept in the framework of the lattice Boltzmann method, and improving the accuracy and efficiency of the simulation by refining the mesh near moving boundaries. Besides elastic boundary with a constitutive law, the method can also efficiently simulate solid moving-boundary interacting with fluid by employing the direct forcing technique. The method is validated by the simulations of flow past a circular cylinder, two cylinders moving with respect to each other and flow around a hovering wing. The versatility of the method is demonstrated by the numerical studies including elastic filament flapping in the wake of a cylinder and fish-like bodies swimming in quiescent fluid. Copyright © 2006 John Wiley & Sons, Ltd.

Received 8 May 2006; Revised 24 August 2006; Accepted 24 August 2006

KEY WORDS: immersed-boundary method; lattice Boltzmann method; multi-block strategy; direct forcing method; moving boundary; fluid–structure interactions

1. INTRODUCTION

Fluid–structure interaction problems are very important in many bio-fluid systems, such as cardiovascular flow, fish locomotion and insect flight. To achieve both accuracy and efficiency in simulating fluid–structure interaction is still a challenge. For numerical methods based on body-fitted grid, such as arbitrary Lagrangian Eulerian (ALE) method [1–3], the mesh is reconstructed with the motion of the structure. It has high-order accuracy but is very computationally expensive. When the boundaries are geometrical irregular or undergoing large deformation, the

*Correspondence to: Hong-Tong Low, Division of Bioengineering, National University of Singapore, 9 Engineering Drive 1, Singapore 117576, Singapore.
†E-mail: mpelowht@nus.edu.sg

re-meshing procedure will be very difficult. For fixed grid methods, re-meshing is not needed; only the variables on the Cartesian mesh near the moving boundary are treated so that the effect of the boundary is considered. These methods are, therefore, more efficient and draw much attention recently.

The immersed-boundary method developed by Peskin [4, 5], to simulate blood flow in the heart, is a kind of fixed grid method. In this method, a force density is distributed to the Cartesian mesh in the vicinity of the moving boundary in order to account for the effect of the boundary. The immersed-boundary method is originally developed for modelling interaction between incompressible viscous fluid and elastic boundary, and the force density is calculated from the boundary's constitutive law. However, it has been extended to deal with solid body by Goldstein *et al.* [6] and Saiki and Biringen [7] by employing a feedback forcing system. The disadvantages of this system are: it causes spurious oscillations and introduces two free parameters which must be determined by the flow conditions. Later, Mohd-Yusof [8] and Fadlun *et al*. [9] proposed the direct forcing method, which has been proved to be more efficient and can be used at higher Reynolds number flows. Distributing force density on a narrow region near the boundary is an inherent feature of the immersed-boundary method. This feature makes it necessary to use fine mesh near the boundary, especially at higher Reynolds number flows.

Recently, lattice Boltzmann method, a kinetic-based approach for simulating fluid flow, has been developed extensively and proven to be a robust and alternative method for solving complex fluid systems [10–13]. The standard lattice Boltzmann method, which employs a uniform Cartesian mesh, has been combined with immersed-boundary method by Feng and Michaelides [14, 15] for solving rigid particles flow. However, it is difficult to extend the immersed-boundary lattice Boltzmann method (IBLBM) to flow problems with high Reynolds number, mainly because high grid resolution is needed near the solid boundary; as the method employs uniform mesh, the computational effort would be very large. Filippova and Hänel [16] and Yu *et al*. [17] have proposed the multi-block lattice Boltzmann method, in which the computational domain is divided into blocks: fine mesh covers the blocks in which the gradients are large and coarse mesh is employed for other blocks. The computational efficiency of lattice Boltzmann method has been substantially improved by the multi-block strategy.

In the present paper, the immersed-boundary method is employed in the framework of multi-block lattice Boltzmann method to model the interactions between incompressible viscous fluid and moving solid or elastic boundaries. For solid boundary immersed in fluid, the direct forcing scheme has been employed. Fine mesh is used only near the moving boundaries, which makes the simulation efficient and accurate. Flow past circular cylinder, two cylinders moving with respect to each other and flow around a hovering wing have been calculated to validate our algorithm. The simulation of an elastic filament flapping in the wake of a cylinder is carried out to demonstrate the capability of the method for fluid and elastic-boundary interaction problem. The method has also been applied to simulate fish-like bodies swimming in fluid as an example of interaction between complex solid boundaries.

2. NUMERICAL METHOD

2.1. Multi-block lattice Boltzmann method

The lattice Boltzmann method is a kinetic-based approach for simulating fluid flows. It decomposes the continuous fluid flow into pockets of fluid particles which can only stay at rest or move to one

DOI: 10.1002/fld

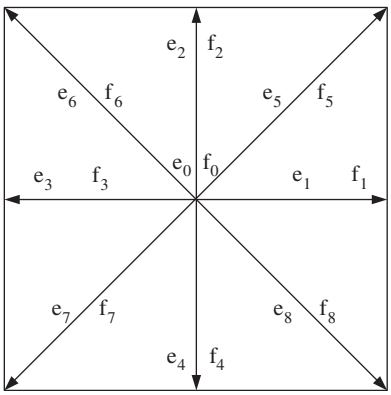

Figure 1. D2Q9 lattice model.

of the neighbouring nodes. The D2Q9 model using a square lattice with nine possible velocities (see Figure 1) is one of the commonly used models in two-dimensional simulation, in which the discrete lattice Boltzmann equation (LBE) has the form of [18]:

$$f_i(\mathbf{x}+\mathbf{e}_i\Delta t, t+\Delta t) - f_i(\mathbf{x}, t) = -\frac{1}{\tau}[f_i(\mathbf{x}, t) - f_i^{\mathrm{eq}}(\mathbf{x}, t)] \tag{1}$$

where $f_i(\mathbf{x}, t)$ is the distribution function for particles with velocity $\mathbf{e}_i$ at position $\mathbf{x}$ and time t, Δt is the lattice time interval, $f_i^{\mathrm{eq}}(\mathbf{x}, t)$ is the equilibrium distribution function and τ is the non-dimensional relaxation time.

In the D2Q9 model, the fluid particles have the possible discrete velocities stated as follows:

$$\begin{aligned}
&\mathbf{e}_0 = (0, 0)\\
&\mathbf{e}_i = (\cos[\pi(i-1)/2], \sin[\pi(i-1)/2])c \quad \text{for } i = 1\text{–}4\\
&\mathbf{e}_i = \sqrt{2}(\cos[\pi(i-9/2)/2], \sin[\pi(i-9/2)/2])c \quad \text{for } i = 5\text{–}8
\end{aligned} \tag{2}$$

where $c = \Delta x/\Delta t$ and Δx is the lattice spacing.

The equilibrium distribution function $f_i^{\mathrm{eq}}(\mathbf{x}, t)$ is in the form of:

$$f_i^{\mathrm{eq}} = E_i(\rho, \mathbf{u}) \tag{3}$$

with

$$E_i(\rho, \mathbf{u}) = \omega_i \rho \left[1 + \frac{\mathbf{e}\cdot\mathbf{u}}{c_s^2} + \frac{\mathbf{uu} : (\mathbf{e}_i\mathbf{e}_i - c_s^2\mathbf{I})}{2c_s^4}\right] \tag{4}$$

where ω_i are the weighing factors with the values

$$\begin{aligned}
&\omega_0 = 4/9\\
&\omega_i = 1/9 \quad \text{for } i = 1\text{–}4\\
&\omega_i = 1/36 \quad \text{for } i = 5\text{–}8
\end{aligned} \tag{5}$$

and $c_s = c/\sqrt{3}$ is the sound speed.

DOI: 10.1002/fld

The relaxation time is related to the kinematic viscosity in Navier–Stokes equation in the form of

$$v = \left(\tau - \frac{1}{2}\right) c_s^2 \Delta t \tag{6}$$

Once the particle density distribution is known, the fluid density and momentum are calculated, using

$$\rho = \sum_i f_i \tag{7}$$

$$\rho \mathbf{u} = \sum_i \mathbf{e}_i f_i \tag{8}$$

In the present paper, the multi-block lattice Boltzmann method proposed by Yu *et al*. [17] is employed. The computational domain is divided into blocks which are connected through the interface. In each block, the constant lattice spacing equals the lattice time interval. On the interface between blocks, the exchange of variables follows a certain relation so that the mass and momentum are conserved and the stress is continuous across the interface.

Consider a two-block system to explain the idea of the multi-block method. The ratio of lattice space between the two blocks is defined as follows:

$$m = \frac{\Delta x_c}{\Delta x_f} \tag{9}$$

where Δx_c and Δx_f are the lattice space of the coarse- and fine-mesh blocks, respectively. For a given lattice space, the fluid viscosity can be obtained from Equation (6). In order to keep a constant viscosity, the relaxation parameter τ_f in fine mesh and τ_c in coarse mesh, must satisfy the following relation:

$$\tau_f = \tfrac{1}{2} + m(\tau_c - \tfrac{1}{2}) \tag{10}$$

The variables and their derivatives on the grid must be continues across the block interface. To keep this continuity, the relation of the density distribution function in the neighbouring blocks is proposed as:

$$\tilde{f}_i^c = f_i^{eq,f} + m\frac{\tau_c - 1}{\tau_f - 1}[\tilde{f}_i^f - f_i^{eq,f}] \tag{11}$$

$$\tilde{f}_i^f = f_i^{eq,c} + \frac{\tau_f - 1}{m(\tau_c - 1)}[\tilde{f}_i^c - f_i^{eq,c}] \tag{12}$$

where $\tilde{f}_i$ is the post-collision density distribution function.

The typical structure of interface is illustrated in Figure 2. The fine block boundary, line MN, is in the interior of the coarse block. The coarse block boundary, line AB, is in the interior of the fine block. This arrangement is convenient for information exchange. On the boundary of fine block MN, there is no information on the grid points denoted by the solid symbol • in Figure 2. It is obtained from spatial interpolation based on the information on the grid nodes denoted by the open symbol ∘ on the line MN. A symmetric, cubic spline spatial fitting [17] is used to avoid

DOI: 10.1002/fld

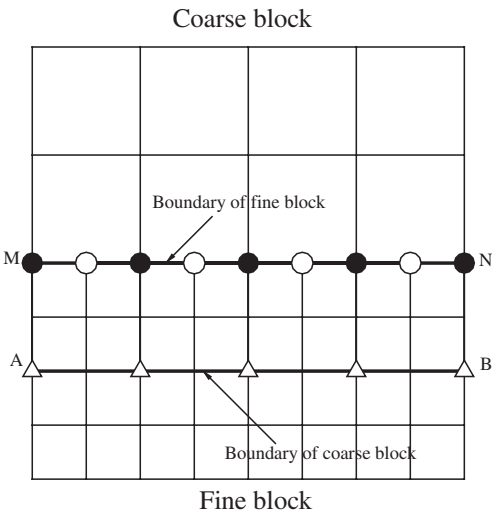

Figure 2. Interface structures between two blocks.

spatial asymmetry caused by interpolation

$$\tilde{f}(x) = a_i + b_i x + c_i x^2 + d_i x^3, \quad x_{i-1} \leqslant x \leqslant x_i, \quad i = 1, \ldots, n \tag{13}$$

where the constants (a_i, b_i, c_i, d_i) are determined by using the continuity conditions of f, f', f'' and suitable end conditions such as zero second derivatives for f.

Because the fluid particle has the same streaming velocity on each block, the computation marches m steps on the fine-mesh block for every one step on the coarse-mesh block. On the fine block MN, temporal interpolation is needed to obtain $\tilde{f}_\alpha(t^{(n+1)/m}, \mathrm{MN})$. A three-point Lagrangian formula [17] is used for temporal interpolation,

$$y(t) = \sum_{k=1}^{3} y_k \left(\prod_{\substack{j=1 \\ j \neq k}} \frac{t - t_i}{t_k - t_j} \right) \tag{14}$$

2.2. *Immersed-boundary method*

In the immersed-boundary method of Peskin [4, 5], two different sets of coordinate system are used. The fluid region is represented by fixed Cartesian grids and the moving boundary immersed in the fluid is decomposed into a set of Lagrangian points. The Lagrangian points are advected by the flow field. The fluid–structure interaction is modelled by adding a force term to the right-hand side of the Navier–Stokes equation which governs the fluid motion.

To explain the immersed-boundary method, we consider a massless elastic filament with boundary Γ immersed in the fluid domain Ω (see Figure 3). The fluid domain Ω is represented by Eulerian coordinates $\mathbf{x}$, while the boundary of the filament Γ, is represented by Lagrangian coordinates $\mathbf{s}$. Any position on the filament can be written as $\mathbf{X}(\mathbf{s}, t)$; $\mathbf{F}(\mathbf{s}, t)$ represents the filament

DOI: 10.1002/fld

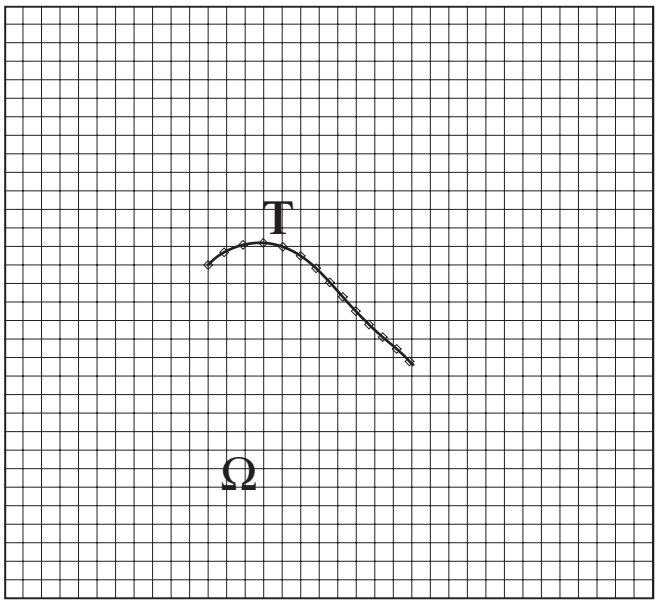

Figure 3. An elastic boundary immersed in fluid.

force density, which is a combination of internal link force induced by deformation and external force and $\mathbf{f}(\mathbf{x}, t)$ represents the fluid body force density.

The non-slip boundary condition is satisfied by letting the flexible structure move at the same velocity as the fluid around it. That is,

$$\frac{\partial \mathbf{X}(\mathbf{s}, t)}{\partial t} = \mathbf{u}(\mathbf{X}(\mathbf{s}, t), t) \tag{15}$$

This motion will cause the filament to deform. The boundary force density $\mathbf{F}(\mathbf{s}, t)$ is obtained from the constitutive law of the filament, and distributed to the fluid mesh points near it by a Dirac Delta function, written as follows:

$$\mathbf{f}(\mathbf{x}, t) = \int_{\Gamma} \mathbf{F}(\mathbf{s}, t)\delta(\mathbf{x} - \mathbf{X}(\mathbf{s}, t))\, \mathrm{d}\mathbf{s} \tag{16}$$

where

$$\delta(r) = \begin{cases} \dfrac{1}{4}\left(1 + \cos\left(\dfrac{\pi|r|}{2}\right)\right), & r \leqslant 2 \\ 0, & r > 2 \end{cases} \tag{17}$$

in which r is the distance between the Lagrange and Eulerian nodes divided by the Eulerian grid space. For two-dimensional case, the Dirac Delta function can be written as follows:

$$\delta(\mathbf{X} - \mathbf{X}_{ij}) = \delta(x - x_{ij})\delta(y - y_{ij}) \tag{18}$$

DOI: 10.1002/fld

The same Dirac Delta function is used to obtain the velocities of the Lagrangian nodes on the moving boundary. The mathematical form can be written as follows, which illustrates the implementation of Equation (15):

$$\frac{\partial \mathbf{X}}{\partial t} = \int_{\Omega} \mathbf{u}(\mathbf{x}, t)\delta(\mathbf{x} - \mathbf{X}(\mathbf{s}, t))\, \mathrm{d}\mathbf{x} \tag{19}$$

The immersed-boundary method is originally developed for modelling interaction between incompressible viscous fluid and elastic boundary with a constitutive law. However, it has been extended to solve solid body immersed in fluid by several researchers. The key procedure is how to generate the force density. Goldstein *et al*. [6] and Saiki and Biringen [7] proposed a feedback forcing system. However, it causes spurious oscillations and introduces two free parameters which must be determined by the flow conditions.

Mohd-Yusof [8] and Fadlun *et al*. [9] proposed the direct forcing method, which has been proved to be more efficient and can be used at higher Reynolds number flows. The Navier–Stokes equation with a force density in discrete form is written as follows:

$$\rho\left(\frac{u_i^{n+1} - u_i^n}{\Delta t} + u_j^n u_{j,i}^n\right) = -p_{,i}^n + \mu u_{i,jj}^n + \mathbf{f}_i^{n+1} \tag{20}$$

If the boundary condition at $t = t^{n+1}$ can be imposed, the force density can be directly obtained from

$$\mathbf{f}_i^{n+1} = \rho\left(\frac{u_i^{n+1} - u_i^n}{\Delta t} + u_j^n u_{j,i}^n\right) + p_{,i}^n - \mu u_{i,jj}^n \tag{21}$$

Recently, Feng and Michaelides [15] have proposed a new direct forcing scheme, in which at $t = t^{n+1}$ the velocity at the Lagrangian point equals the velocity of the solid boundary at the same point, U_i^{n+1}. Thus, the force density is calculated from

$$\mathbf{f}_i^{n+1} = \rho\left(\frac{U_i^{n+1} - u_i^n}{\Delta t} + u_j^n u_{j,i}^n\right) + p_{,i}^n - \mu u_{i,jj}^n \tag{22}$$

This scheme is more efficient for moving-boundary problems.

2.3. Hybrid immersed-boundary and multi-block lattice Boltzmann method

In the present paper, the immersed-boundary method is combined with the multi-block lattice Boltzmann method. In order to solve the flow field with a force density, the LBE must be modified. Several forms of LBE which can handle a force density have been proposed. Guo *et al*.'s approach [19] is more accurate for unsteady flow with force changing with time and space, in which the modified LBE is in the following form:

$$f_i(\mathbf{x} + \mathbf{e}_i \Delta t, t + \Delta t) - f_i(\mathbf{x}, t) = -\frac{1}{\tau}[f_i(\mathbf{x}, t) - f_i^{\mathrm{eq}}(\mathbf{x}, t)] + \Delta t F_i \tag{23}$$

DOI: 10.1002/fld

where

$$f_i^{\mathrm{eq}} = E_i(\rho, \mathbf{u}^*) \tag{24}$$

with

$$\rho \mathbf{u}^* = \sum_i \mathbf{e}_i f_i + \frac{1}{2}\mathbf{f}\Delta t \tag{25}$$

$$F_i = \left(1 - \frac{1}{2\tau}\right) \omega_i \left[\frac{\mathbf{e}_i - \mathbf{u}}{c_{\mathrm{s}}^2} + \frac{(\mathbf{e}_i \cdot \mathbf{u})}{c_{\mathrm{s}}^4}\mathbf{e}_i\right] \cdot \mathbf{f} \tag{26}$$

In the computation, a two-grid system is employed. The lattice space ratio between coarse and fine grid is equal to 2. The solid or elastic boundaries are immersed in the fine-mesh block. The present procedure for multi-block computation is very similar to that proposed by Yu *et al*. [17]. The only difference exists in the computation on the fine-mesh block. That is a subroutine implementing the immersed-boundary method is added before the streaming and collision steps.

3. RESULTS AND DISCUSSION

3.1. Flow passing a circular cylinder

The flow past a circular cylinder is a standard benchmark computation for testing many numerical methods. This case is used to validate our method for solving fluid–solid boundary problem. The Reynolds number, drag coefficient, lift coefficient and Strouhal number are defined as

$$\begin{aligned} Re &= \frac{\rho U_\infty D}{\mu} \\ C_{\mathrm{d}} &= \frac{F_{\mathrm{d}}}{0.5\rho U_\infty^2 D} \\ C_{\mathrm{l}} &= \frac{F_{\mathrm{l}}}{0.5\rho U_\infty^2 D} \\ St &= \frac{f D}{U_\infty} \end{aligned} \tag{27}$$

where ρ is the fluid density, μ is the fluid viscosity, U_∞ is the incoming velocity, D is the diameter of the cylinder, F_{d} and F_{l} are the drag and lift forces, and f is the oscillation frequency.

The flow is computed at Reynolds number of 100 and 200 using computational domain of 30×20. The diameter of the cylinder is 1 and its centre is located at [10, 10]; $\rho = 1$, $U_\infty = 0.1$. The mesh and block system is illustrated in Figure 4. The fine-mesh block covers the area from 8 to 16 on x-axis and 8 to 12 on y-axis, which is about 5.3% of the whole computational domain by area. In the fine block, $\Delta x_{\mathrm{f}} = \Delta y_{\mathrm{f}} = \Delta t_{\mathrm{f}} = 0.02$. The other area is covered by coarse-mesh blocks, in which $\Delta x_{\mathrm{c}} = \Delta y_{\mathrm{c}} = \Delta t_{\mathrm{c}} = 0.04$. On the far-field boundary, the density distribution function is set at its equilibrium state.

DOI: 10.1002/fld

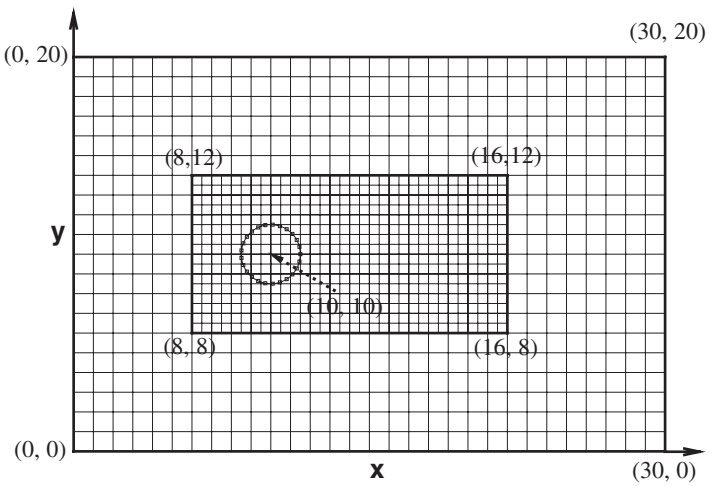

Figure 4. Illustration of mesh and block system on the computational domain. Mesh density is reduced by a factor of 25 for clarity.

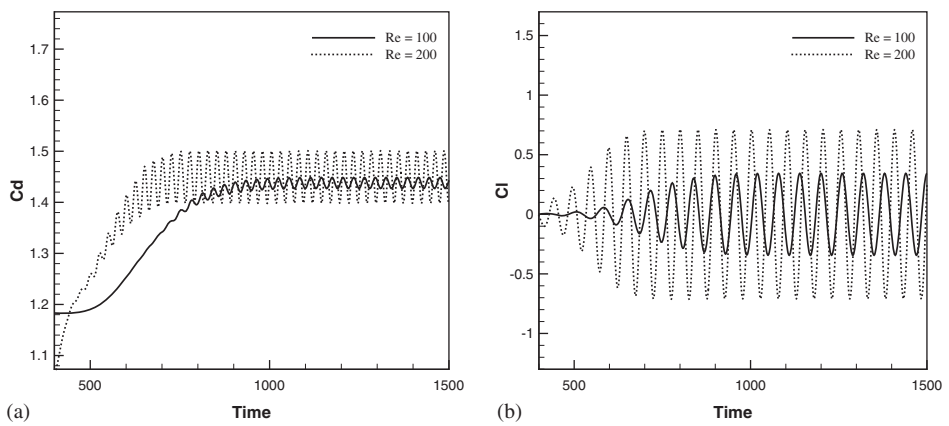

Figure 5. Evolution of force coefficients: (a) drag; and (b) lift.

In Figures 5(a) and (b) the evolution history of drag and lift coefficients is presented. The oscillation frequency of drag is twice that of lift. The stream function and pressure contours are presented in Figures 6(a) and (b), and 7(a) and (b). In Figures 8(a) and (b) the vorticity contour around the cylinder is presented. The Karman vortex street is observed in the wake. From Figures 6–8, it is clear that the variables at the interface between blocks are continuous.

The drag coefficient, lift coefficient and Strouhal number are compared with that of previous literatures in Table I. It shows that the present results are within the range of values reported by previous studies.

DOI: 10.1002/fld

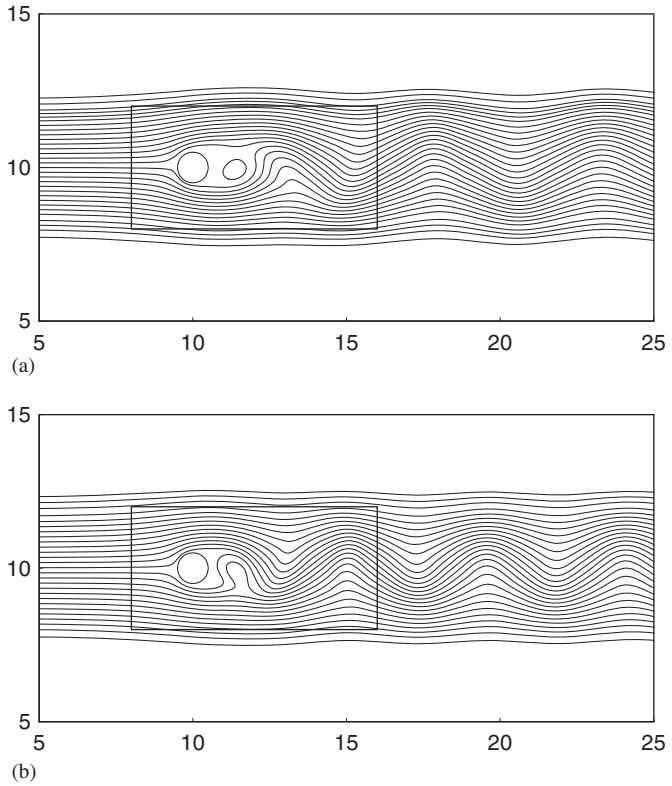

Figure 6. Stream function contour: (a) $Re = 100$; and (b) $Re = 200$.

To demonstrate that the results are grid-independent, numerical simulation for several grids with different sizes were carried out, with the same two-block system. The drag coefficient is used as an indicator for this study. From the results in Table II, the grid resolution of $\Delta x_f = \Delta y_f = 0.02$ is sufficient to capture the important characteristics.

With a fine-mesh system covering the whole computational domain, which is actually the original IBLBM, a numerical study is carried out on flow past a cylinder at $Re = 100$. The drag coefficient, lift coefficient and Strouhal number are found to be 1.436, 0.343 and 0.166, respectively, which are nearly the same as that of the present multi-block method. However, only about 5.3% of the computational area is covered by fine mesh with the present multi-block method. Computational effort is saved by using less mesh, and furthermore one time step on coarse mesh needs two time steps in fine-mesh. The computational effort saved is estimated as follows:

$$1 - \frac{(5.3\% \times 2 + 0(\text{ib})) \times 2 + (100\% - 5.3\%)}{(100\% \times 2 + 0(\text{ib})) \times 2} \approx 0.71$$

where 0(ib) is the computational effort incurred by implementing the immersed-boundary condition, which is a small value compared with the fluid field computation effort. Conversely, it can be

DOI: 10.1002/fld

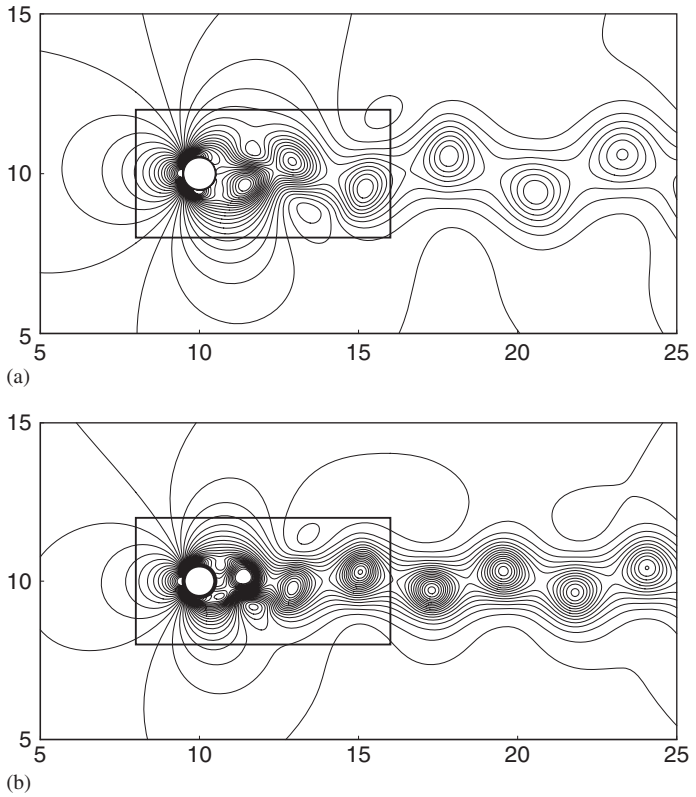

Figure 7. Pressure contours: (a) $Re = 100$; and (b) $Re = 200$.

expected that under the same computational effort, the present method gives more accurate result as the near boundary region is covered with fine-mesh.

3.2. Two circular cylinders moving with respect to each other

This example is used to test the present method in simulating solid moving boundaries immersed in fluid. It has been previously studied by Russell and Wang [21], as well as Xu and Wang [22]. The initial geometry (Figure 9) is the same as theirs, and so is the far-field rigid wall boundary condition. The fine-mesh block, with bold solid line as the boundary in Figure 9, covers the area from -3 to 19 on x-axis and -2 to 3.6 on y-axis. The other area is covered with coarse mesh. The grid resolutions in both blocks are the same as that in Section 3.1. The diameter of both cylinders is equal to 1, which is also the characteristic length. Each cylinder, oscillates for two periods about its initial position and then moves with respect to each other at the characteristic velocity $U = 0.025$ and $Re = 40$. Compared with Xu and Wang [22] the same characteristic length is used, however, the current characteristic velocity is $\frac{1}{40}$ of their study; so the time scale is

DOI: 10.1002/fld

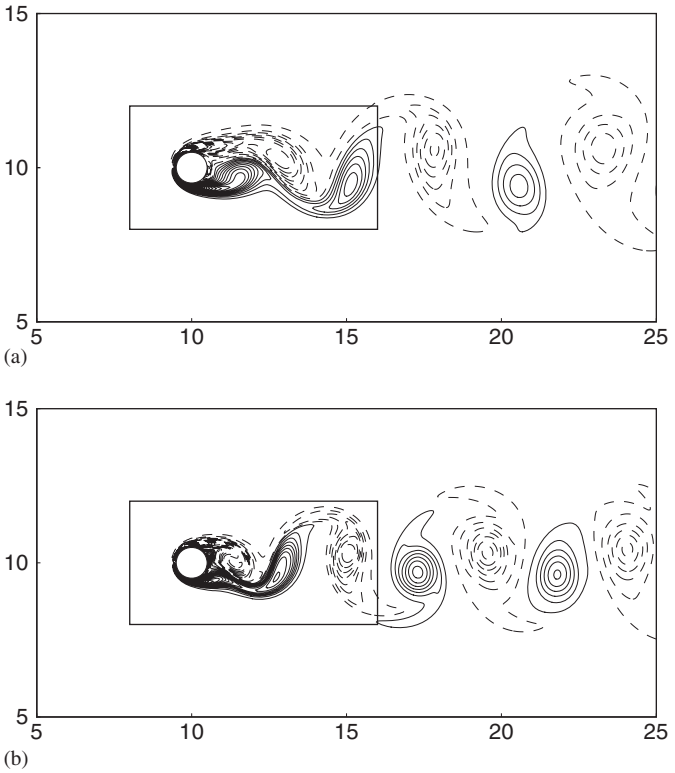

Figure 8. Vorticity contours: (a) $Re = 100$; and (b) $Re = 200$.

Table I. Comparison with previous studies on flow past a circular cylinder.

	$Re = 100$			$Re = 200$		
	C_d	C_l	St	C_d	C_l	St
Lai and Peskin [20]	1.4473	0.3299	0.165	—	—	0.190
Russell and Wang [21]	1.43	0.339	0.175	1.45	0.75	0.202
Xu and Wang [22]	1.423	0.34	0.171	1.42	0.66	0.202
Chew *et al*. [29]	1.3668	0.375	0.164	—	—	—
Present	1.438	0.344	0.166	1.449	0.709	0.197

40 times of theirs. The position of the upper cylinder is

$$x_u = \begin{cases} 16 - \dfrac{4}{\pi} \sin\left(\dfrac{\pi t}{160}\right), & 0 \leqslant t \leqslant 640 \\ 32 - 0.025t, & 640 \leqslant t \leqslant 1280 \end{cases} \qquad (28)$$

$$y_u = 1.5$$

DOI: 10.1002/fld

Table II. Drag coefficients for different grid size.

Grid resolution in fine block	$Re = 100$	$Re = 200$
$\frac{1}{30}$	1.454	1.459
$\frac{1}{40}$	1.443	1.451
$\frac{1}{50}$	1.438	1.449
$\frac{1}{60}$	1.436	1.448
$\frac{1}{70}$	1.435	1.448

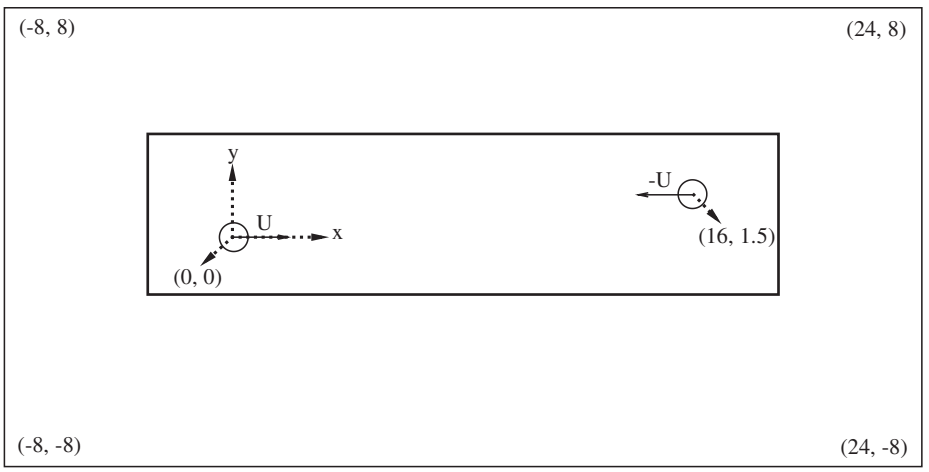

Figure 9. Computational geometry for two cylinders moving with respect to each other.

The position of the lower cylinder is

$$x_1 = \begin{cases} \dfrac{4}{\pi} \sin\left(\dfrac{\pi t}{160}\right), & 0 \leqslant t \leqslant 640 \\ 0.025t - 16, & 640 \leqslant t \leqslant 1280 \end{cases} \qquad (29)$$

$$y_1 = 0$$

A non-equilibrium extrapolation method proposed by Guo *et al.* [23] has been used to treat the rigid wall boundary condition in this section as well as Sections 3.3 and 3.5.

Figure 10(a) presents the vorticity contour when the two cylinders are closest to each other, at $t = 960$; Figure 10(b) shows the vorticity field at $t = 1280$, when the cylinders are separated from each other by a distance of 16. These results qualitatively agree with that of Xu and Wang [22].

DOI: 10.1002/fld

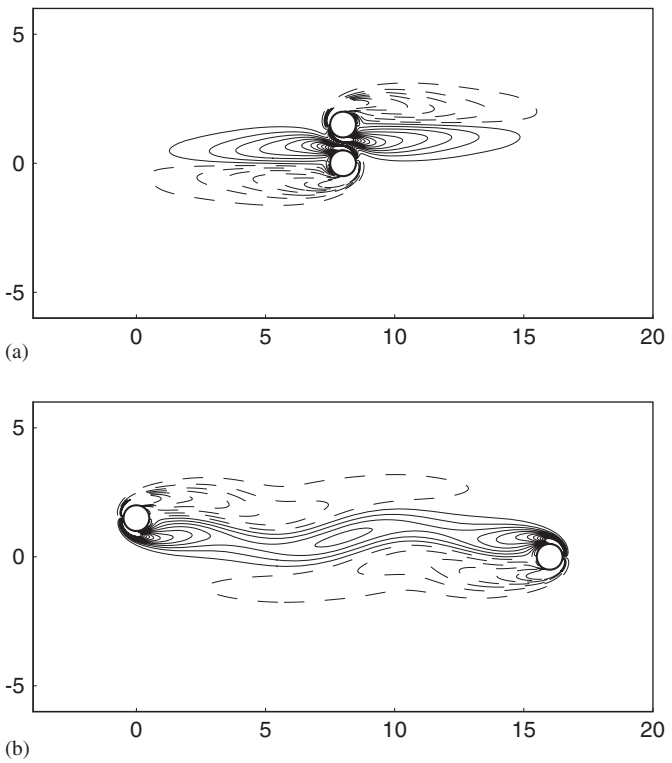

Figure 10. Vorticity fields around two cylinders moving with respect to each other: (a) cylinders are closest to each other; and (b) cylinders are separated by a distance of 16.

The developing history of the drag and lift coefficients of the upper cylinder is shown in Figures 11(a) and (b), using the same time scale as Xu and Wang [22]. Very good quantitative agreement is observed. From the results it is seen that the drag force increases when the two cylinders are approaching each other, which means they are repulsive. However, they are attracting each other when they move away in close proximity, because the drag force decreases.

This case is further studied with the original IBLBM, which employs uniform mesh for the whole computational domain. The grid resolution (IBLBM) is the same as that of the fine block in this section. The temporal evolution of drag and lift coefficients is shown in Figures 11(a) and (b). It is seen that they are nearly the same as the results by the present multi-block method. However, only 24.1% of the computational domain is covered by fine mesh in the current method; thus, computational effort is saved, though not as much as that of Section 3.1.

3.3. Flow around a hovering wing

A rigid wing undergoing both translational and rotational motion within a rigid box is studied as a more stringent case to validate the present method. The wing has an elliptical shape with chord

DOI: 10.1002/fld

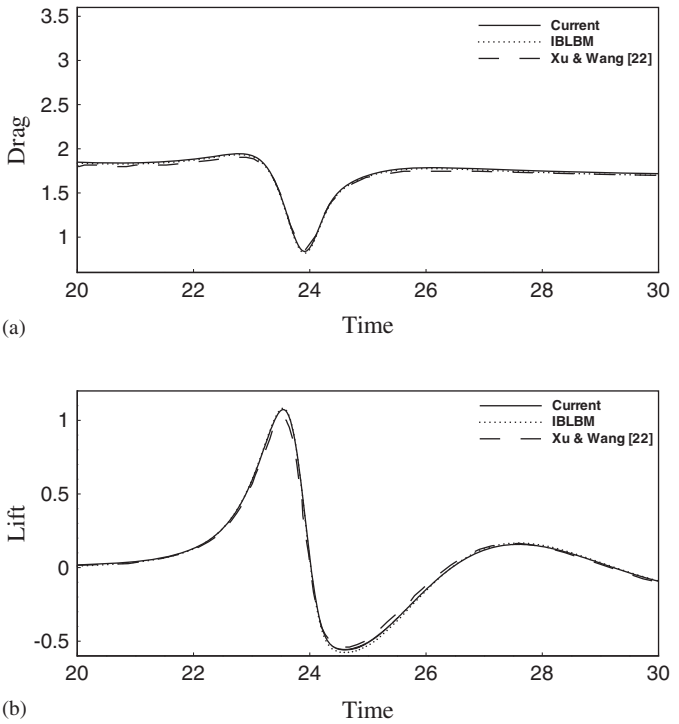

Figure 11. Temporal evolution of: (a) lift; and (b) drag coefficients for the upper cylinder in flow around two cylinders moving with respect to each other.

length c and aspect ratio e. Its positions in one period are shown in Figure 12. Mathematically, it is governed by

$$A(t) = 0.5A_0\left(1 + \cos\frac{2\pi t}{T}\right)$$
$$\alpha(t) = \alpha_0\left(1 - \sin\left(\frac{2\pi t}{T} - \theta\right)\right) \tag{30}$$

where $A(t)$ is the displacement of the wing centre with amplitude A_0, $\alpha(t)$ is the angle of attack with amplitude $2\alpha_0$, T is the flapping period and θ is the phase difference. The inclination angle of the stroke plane is β (Figure 12). In the present study, the parameters are: $c=1$, $e=4$, $A_0=2.5$, $\alpha_0=\pi/4$, $T=50\pi$, $\theta=0$ and $\beta=\pi/3$. The characteristic length is c, the velocity scale is $\pi A_0/T$ and the Reynolds number is $\pi A_0 c/T\nu$, which is equal to 157. This example has been previously studied by Xu and Wang [22]; the only difference is that the present characteristic velocity is $\frac{1}{20}$ of theirs, and thus the present time scale is 20 times of theirs.

DOI: 10.1002/fld

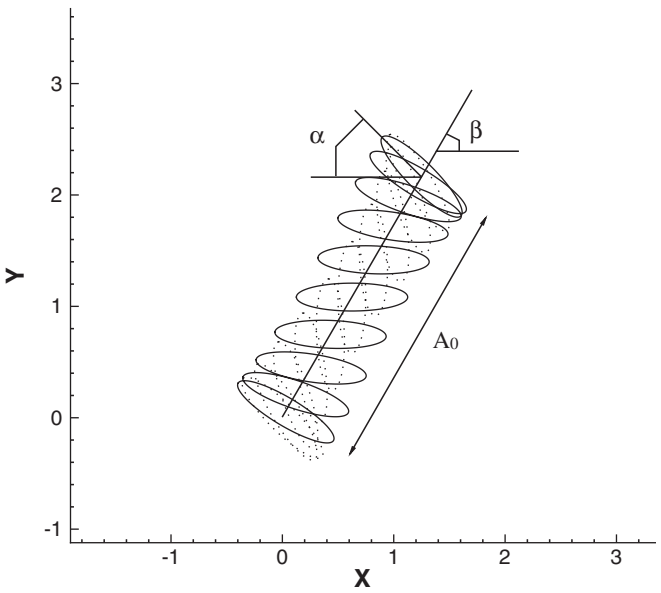

Figure 12. Positions of a hovering wing in one period. The solid ellipses represent the downstroke phase and the dotted ellipses represent the upstroke phase.

The present rigid box ranges from -10 to 6 on both x-axis and y-axis, which is also the computational domain. The fine-mesh system covers the area from 8 to 13 on x-axis and 8 to 14 on y-axis. The other area is covered with coarse mesh. The grid resolutions in fine block are $\Delta x_f = \Delta y_f = \Delta t_f = \frac{1}{64}$, and $\Delta x_c = \Delta y_c = \Delta t_c = \frac{1}{32}$ in coarse block. Further refinement of the mesh gives nearly the same results.

Figure 13 presents four images of the vorticity field near the wing within one period. A pair of vortex with different modes are created and shed from the leading and trailing edges of the wing. The vorticity results are very similar to Xu and Wang [22], and its physical meaning was given in detail by Wang [24].

The temporal evolution of the drag and lift coefficients of the hovering wing is plotted in Figures 14(a) and (b), using the same time scale as Xu and Wang [22]. Reasonable quantitative agreement is observed.

3.4. Filament flapping in the wake of a cylinder

The flapping motion of an elastic filament in the wake of a circular cylinder is studied at the Reynolds number of 100. This case demonstrates the ability of the present method in dealing with interaction between fluid and elastic-boundary with a prescribed constitutive law. The computational domain, far-field boundary condition, location and diameter of the cylinder, fluid density, incoming flow velocity, grid resolutions in fine block and coarse block are all similar to that of Section 3.1. However, the fine-mesh block covers the area from 8 to 21 on x-axis and 8 to 12 on y-axis, which is about 8.7% of the whole computational domain.

DOI: 10.1002/fld

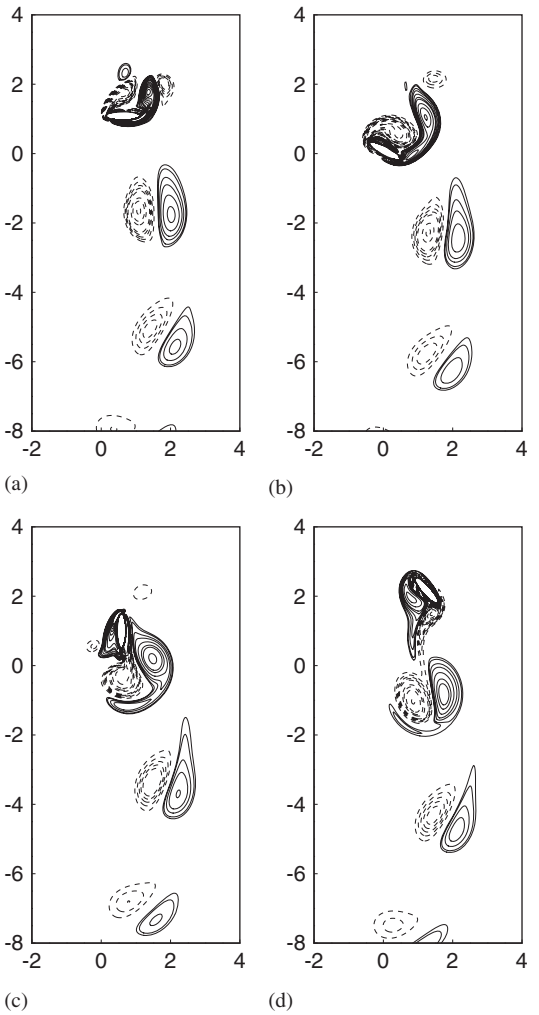

Figure 13. Vorticity fields around a hovering wing at four different instants in a period: (a) $t = 0.25\,T$; $t = 0.44\,T$; (c) $t = 0.74\,T$; and (d) $t = 0.99\,T$.

The constitutive law of the filament is Hook's law, described as follows:

$$\tau = K\left(\frac{\partial \mathbf{X}}{\partial \mathbf{s}} - 1\right) \tag{31}$$

The bending effect of the filament is also considered, with the bending energy E_b defined as

$$E_\mathrm{b} = \frac{1}{2} K_\mathrm{b} \int \left| \frac{\partial^2 \mathbf{X}(\mathbf{s}, t)}{\partial \mathbf{s}^2} \right|^2 \mathrm{d}\mathbf{s} \tag{32}$$

DOI: 10.1002/fld

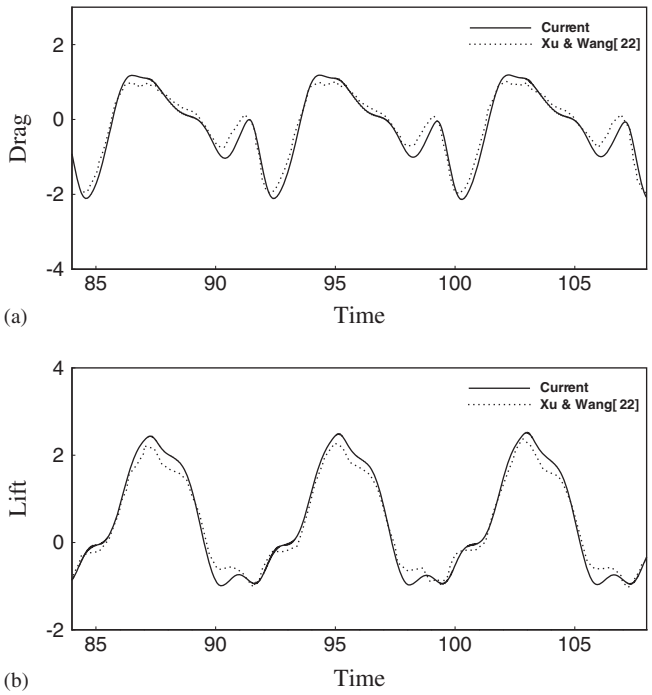

Figure 14. Temporal evolution of: (a) drag; and (b) lift coefficients for flow around a hovering wing at $Re = 157$.

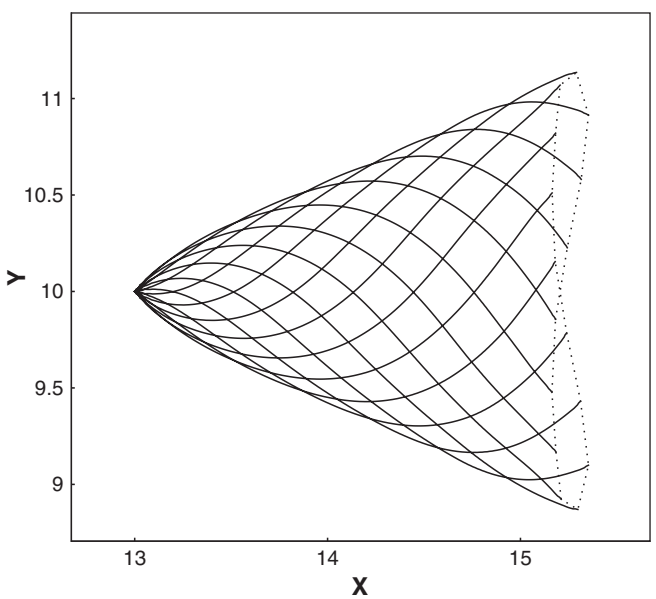

Figure 15. Filament trajectories in one period.

DOI: 10.1002/fld

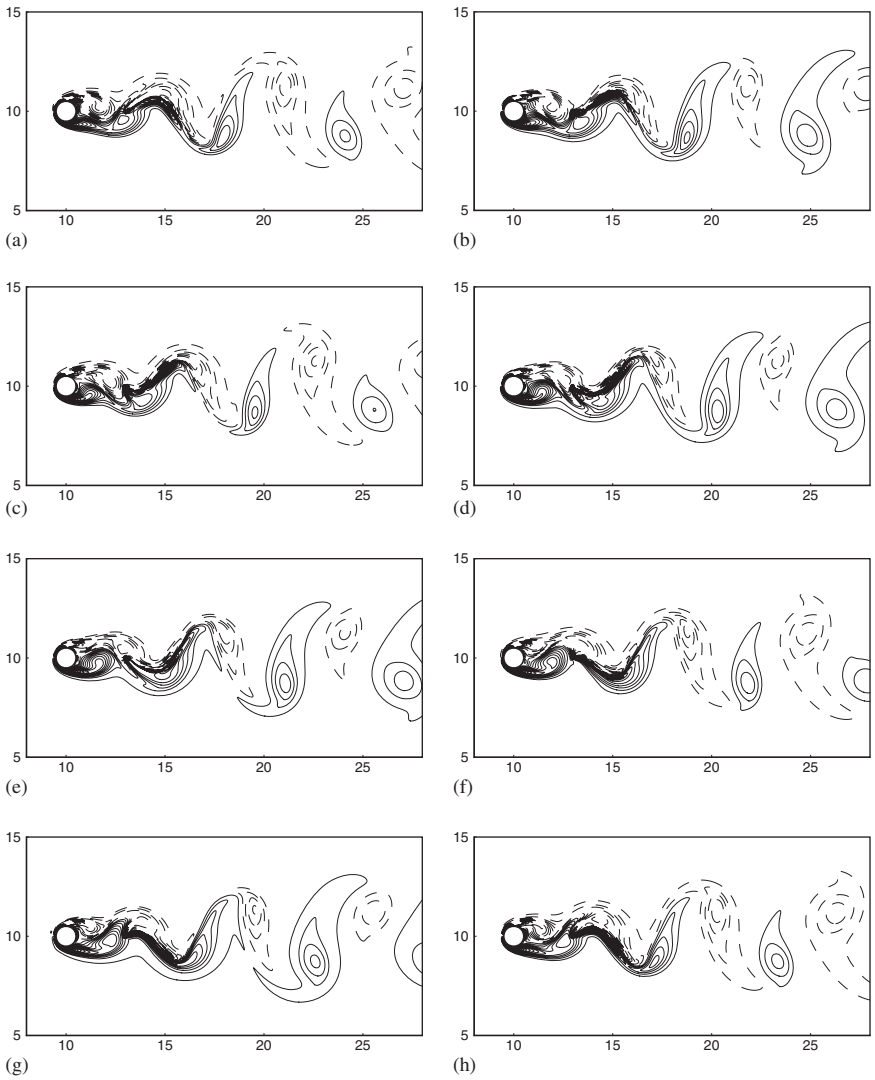

Figure 16. Vorticity contours at different times which are shown in Figure 17.

In the above two equations, τ is filament tension, K is the stretching coefficient which is defined as the ratio between stress and strain. After being scaled by μU_0, the coefficient K takes the value of 5. The coefficient K_b is bending rigidity, defined as the ratio between bending moment and curvature. After being normalized by $\mu U_0 D^2$ (D is cylinder diameter), it is equal to 5×10^{-4}. These coefficient values are chosen so that the filament length is nearly unchanged; however, the values are not too large to make the computation unstable.

The filament has an initial length of 2.5, and is initially located on the centreline of the computational domain, aligned with the x-axis. Only the left end of the filament is fixed at

DOI: 10.1002/fld

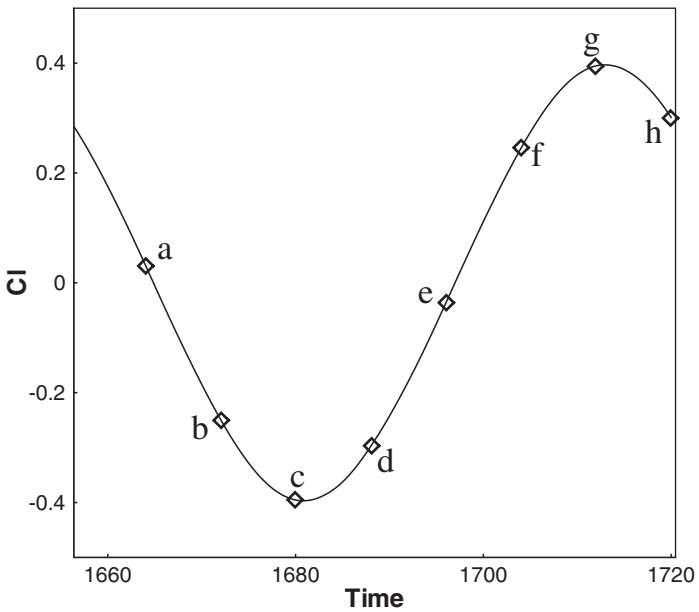

Figure 17. Time sequence of the results shown in Figure 16.

[13, 10] and the other end moves freely with the flow. Shi and Phan-Thien [25] have numerically studied an elastic beam flapping in the wake of a cylinder. In the present study, parameters such as filament length and position are chosen similar to them of the beam in Shi's study.

The results (Figure 15) show that due to the vortex shedding alternately from the upper and lower surfaces of the cylinder, the filament swings periodically in the wake of the cylinder; a sequence of the filament trajectory in one period of swinging is shown. It is interesting that the free end of the filament forms a trajectory with a figure of '8' shape. Similar trajectory shape has been observed by Zhang *et al*. [26] in their experimental study of an elastic filament flapping on a soap film and in Shi's numerical study [25]. A series of vorticity contour during one period is shown in Figure 16, with the time sequence given in Figure 17. It is seen that due to the existence of an elastic filament, the wake flow field has been substantially changed. There are also vortexes shedding from the free tip of the filament. When compared with the vorticity contour without a filament at $Re = 100$ (Figure 8(a)), the shape of Karman vortex street after the cylinder has changed noticeably. The vortices become elongated and the lateral spacing between vortexes is wider.

In order to study the effects of the filament on the characteristics of flow quantitatively, Table III compares the drag coefficient, lift coefficient of the cylinder and the Strouhal number with and without the elastic filament. The results show that due to the flapping motion of the filament, the drag force of the cylinder is decreased. This is because the filament hampers the wake flow. Thus, the pressure is increased in the region between cylinder and filament; and the oscillation of the flow system is slower than that of a single cylinder. From our results (Table III) it is seen that the amplitude of the lift force is increased. To explain its reason, the flow fields nearby the cylinder were studied at the moment when the maximum lift coefficients appear

DOI: 10.1002/fld

Table III. Comparison of flow characteristics for flow past a circular cylinder with and without a downstream filament.

	C_d	C_l	St
Cylinder without filament	1.438	0.344	0.166
Cylinder with filament	1.406	0.396	0.156

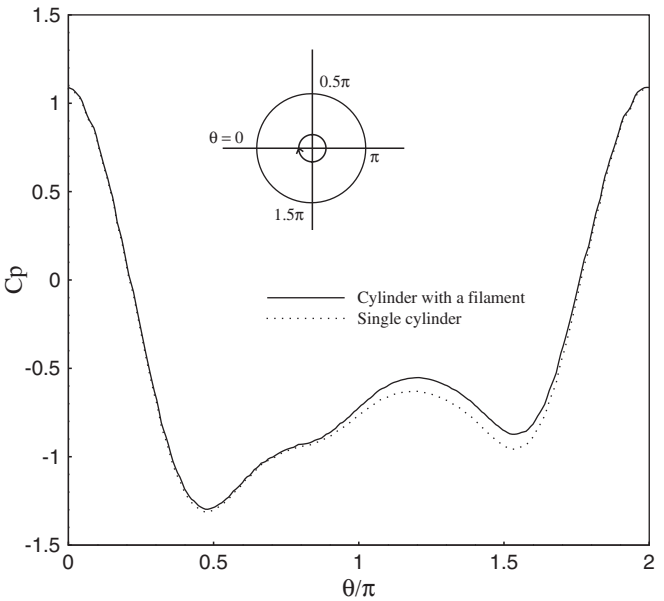

Figure 18. Pressure coefficients along the cylinder surface when the maximum lift coefficients appear.

(0.344 for a single cylinder; 0.396 for a cylinder with a filament). The pressure coefficient, which is defined as $C_p = 0.5(p - p_\infty)/(\rho U_\infty^2)$, are plotted along the cylinder surface ($\theta = 0$ to 2π) in Figure 18. As expected, the existence of the filament increases the pressure in the downstream face of the cylinder, especially the region where θ is between π and 1.5π. It increases the asymmetry of pressure distribution, and therefore increases the lift force. However, as the filament is very flexible, its effect on the upstream cylinder is not large. The changes on these coefficients are about a few percents. Similar trends have also been reported by Shi and Phan-Thien [25].

3.5. Fish-like bodies swimming in fluid

In order to demonstrate the applicability of the method for modelling flexible and complex boundaries moving in incompressible viscous flow, a simulation is made of fish-like bodies swimming in fluid. Two cases are studied: (1) a single fish-like body swimming in fluid at $Re = 400$; (2) two fish-like bodies swimming with respect to each other at $Re = 800$.

The configuration of the fish is approximated by the cross-section of a NACA 0012 airfoil. The fish-like body of length L is moving in a straight line with constant axial velocity U and

DOI: 10.1002/fld

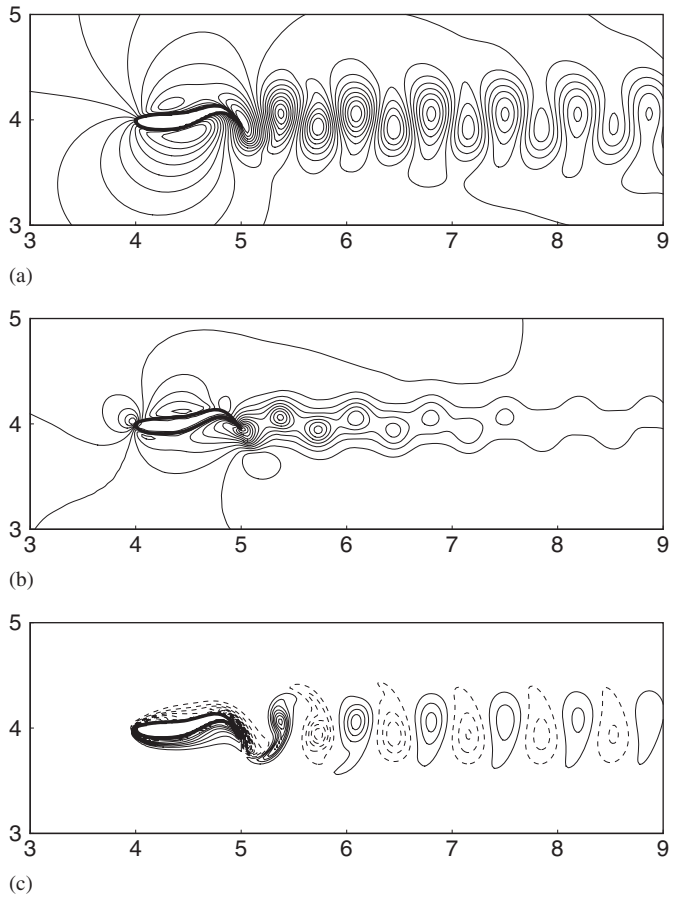

Figure 19. Flwo contours for fish-like body moving in fluid at $Re = 400$, $St = 0.573$ and $t = 140$: (a) stream function; (b) pressure; and (c) voriticity.

undulating in the lateral direction with a prescribed mode. The approach of Gilmanov's [27] is adopted to mimic this undulating motion, in which the lateral displacement of the fish body is described in terms of a travelling wave

$$y(x, t) = a(x) \sin(kx - \omega t), \quad x \in [0, 1] \tag{33}$$

where k is the wave number and ω is the circular frequency of oscillation; and $a(x)$ is the amplitude of the wave, in the form of

$$a(x) = a_0 + a_1 x + a_2 x^2 \tag{34}$$

The constants are chosen as $a_0 = 0.04$, $a_1 = -0.16$, $a_2 = 0.32$, so that $a(x)$ achieves a maximum value of 0.2 at the tail.

DOI: 10.1002/fld

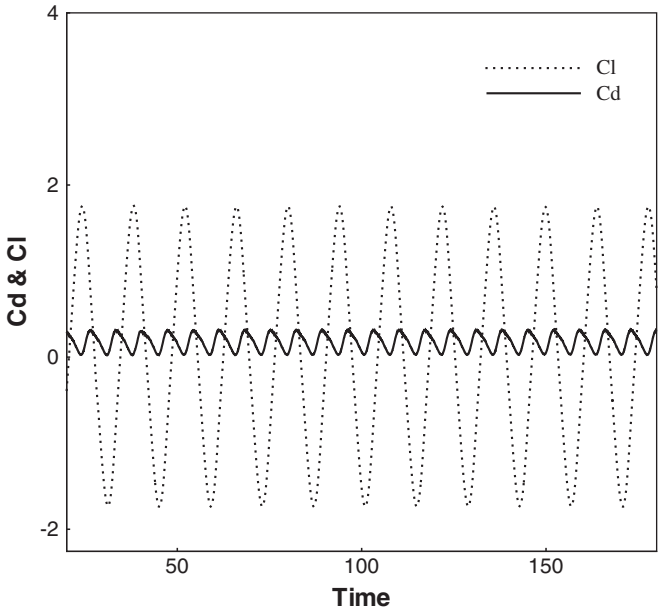

Figure 20. Evolution of the drag and lift coefficients for the fish-like body.

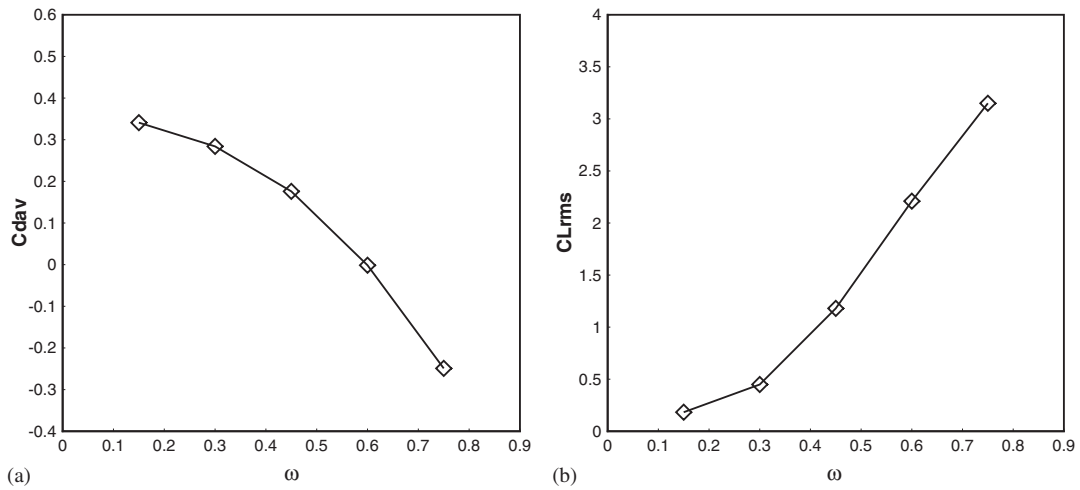

Figure 21. Force coefficients at different circular frequencies: (a) mean drag; and (b) root mean square of lift.

Two important dimensionless numbers are the Reynolds number, defined as $Re = UL/v$, and the Strouhal number, defined as $St = 2a_{\max} f/U$; where f is the undulating frequency and is equal to $\omega/2\pi$, $2a_{\max}$ is the maximum excursion of the tail. In the current study, the parameters are: $L = 1, U = 0.05, Re = 400,$ wave number $k = 2\pi,$ and $\omega = 0.15, 0.30, 0.45, 0.60, 0.75,$ with the

DOI: 10.1002/fld

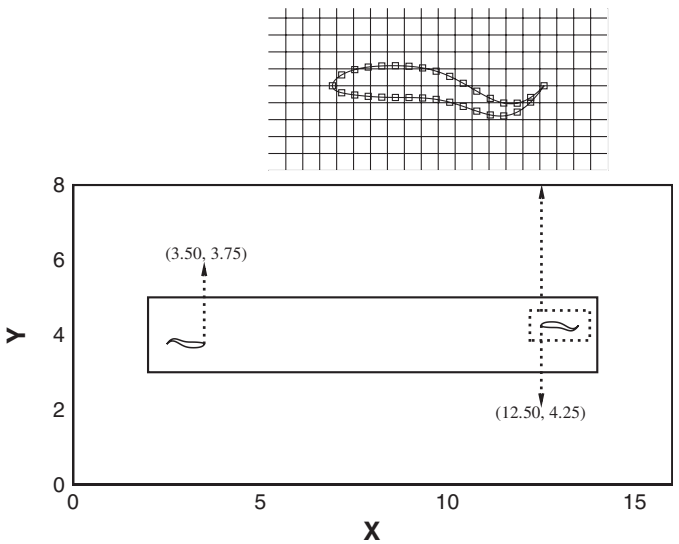

Figure 22. Geometry of two fish-like bodies swimming with respect to each other, with illustration of mesh around the upper fish-like body.

corresponding Strouhal numbers 0.191, 0.382, 0.573, 0.764, 0.955. The computational domain is $[16 \times 8]$ with rigid wall boundary condition; the fine-mesh block covers the area from 2 to 14 on x-axis and 3 to 5 on y-axis, about 18.8% of the whole computational domain by area. In the fine block, $\Delta x_f = \Delta y_f = \Delta t_f = 0.01$. The remaining area is covered by coarse-mesh blocks, in which $\Delta x_c = \Delta y_c = \Delta t_c = 0.02$. In all the cases, the fish-like bodies move within the fine-mesh block.

The simulation of a single fish-like body swimming in a quiescent fluid is presented in Figures 19(a)–(c); the results show the contours of the stream function, pressure and vorticity around the body at $St = 0.573$ and $t = 140$. It is seen that due to the axial and lateral motion of the fish-like body, there are streamlines starting from and ending at the body surface. Vortices with opposite signs are shed periodically from the tail of the fish-like body. A vortex array, very similar to the Von Karman vortex street, is formed in the wake of the moving body. Also studied are the drag and lift coefficients of the fish-like body, whose evolution history are shown in Figure 20. These coefficients are defined in Equation (27), in which the length of the body is chosen as the characteristic length. The result shows that with periodical vortex shedding, both drag and lift coefficients vary periodically. The oscillation frequency of drag is twice that of lift. This trend is similar to that of flow past circular cylinder in Section 3.1.

Also investigated is the effect of the undulating frequency of the fish-like body on the drag and lift coefficients. The motion under different frequencies, $\omega = 0.15$–0.75, with the corresponding Strouhal numbers 0.191–0.955, has been studied. Figures 21(a) and (b) show the mean drag coefficient and the root mean square of lift coefficient at these frequencies. The result shows that the mean drag applied on the fish-like body decreases with the increase in undulating frequency. When the circular frequency ω is approximately greater than 0.6, the mean drag becomes negative which means that it acts as a thrust force. From Figure 20(b) it is seen that with the increase in

DOI: 10.1002/fld

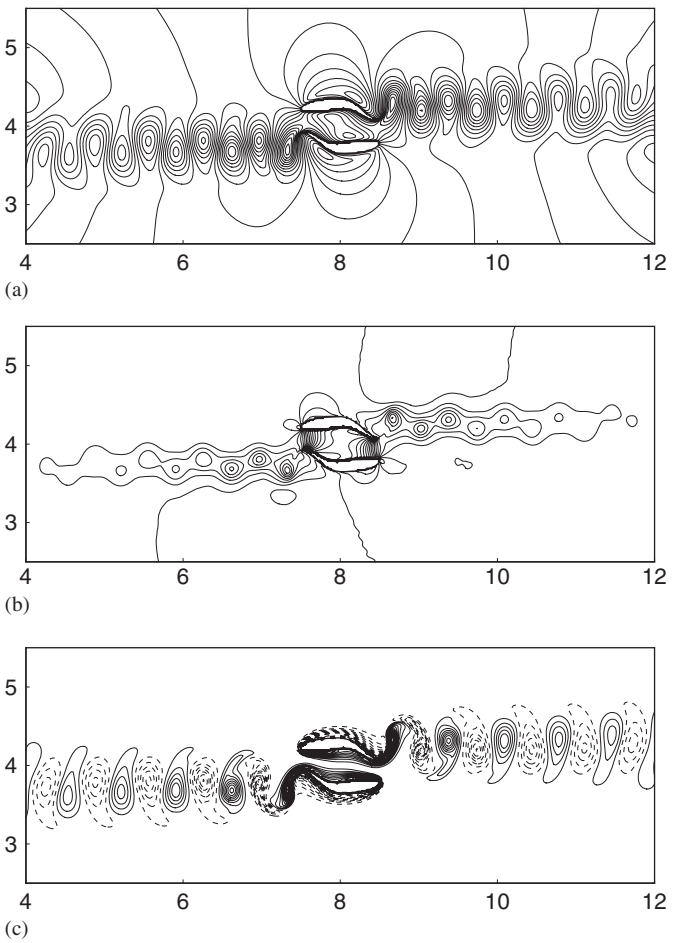

Figure 23. Flow contours for two fish-like bodies moving in fluid at $t = 100$: (a) stream function; (b) pressure; and (c) vorticity.

undulating frequency, the amplitude of the lift increases monotonically. Similar phenomenon has been reported in Dong's study on flow past a fish-like plate with a travelling wave [28].

A simulation was also made of two fish-like bodies swimming with respect to each other. The initial geometry and mesh around the upper fish-like body is illustrated in Figure 22, in which the small rectangular box is the boundary of the fine-mesh block. The fish-like bodies are moving at opposite modes. Figures 23(a)–(c) present the stream function, pressure and vorticity contours at $t = 100$ when the distance between the two bodies is smallest. Figures 24(a)–(c) show the stream function, pressure and vorticity fields when they are further apart, at time $t = 140$. The results show that the vortices shed from the tails of the fish-like bodies and interact with each other, making the flow field very complex. Figure 25 shows the evolution history of the drag and lift coefficients of the upper body. Compared with Figure 19 for a single fish-like body, it is found that the temporal

DOI: 10.1002/fld

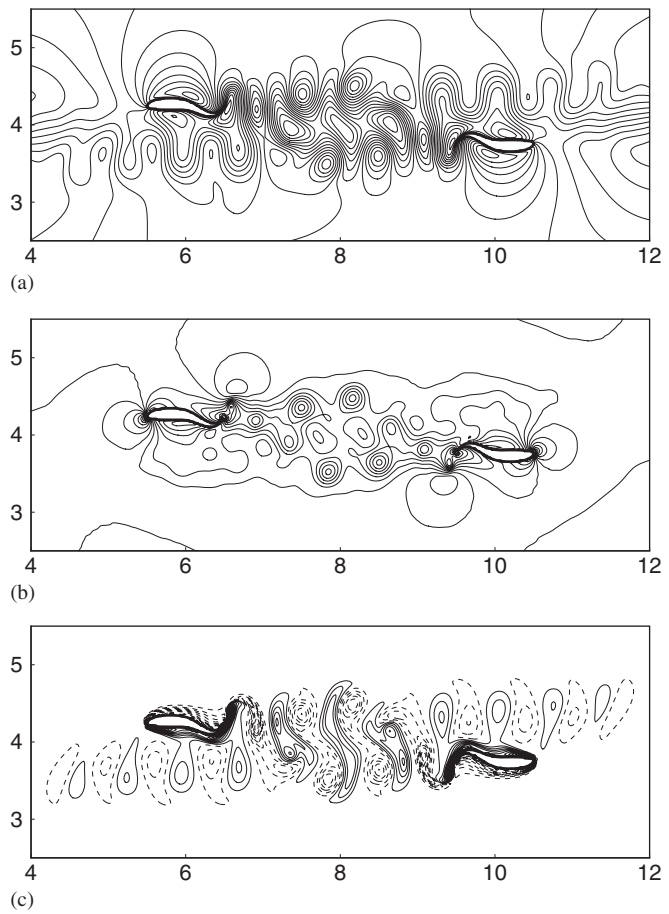

Figure 24. Flow contours for two fish-like bodies mocing in fluid at $t = 140$: (a) stream function; (b) pressure; and (c) vorticity.

evolution of the drag and lift coefficients has changed significantly when these two fish-like bodies are close to each other.

4. CONCLUSIONS

A hybrid immersed-boundary and multi-block lattice Boltzmann method is presented to simulate moving boundaries interacting with incompressible viscous fluid. The present method preserves the advantages of the immersed-boundary method and lattice Boltzmann method; and at the same time improves their accuracy and efficiency by employing a multi-block strategy. Besides dealing with elastic boundaries interacting with fluid, the method can also efficiently simulate solid moving boundaries; this is achieved by employing the direct forcing technique. Three benchmark computations were carried out to validate the present method: flow past a circular cylinder, two cylinders

DOI: 10.1002/fld

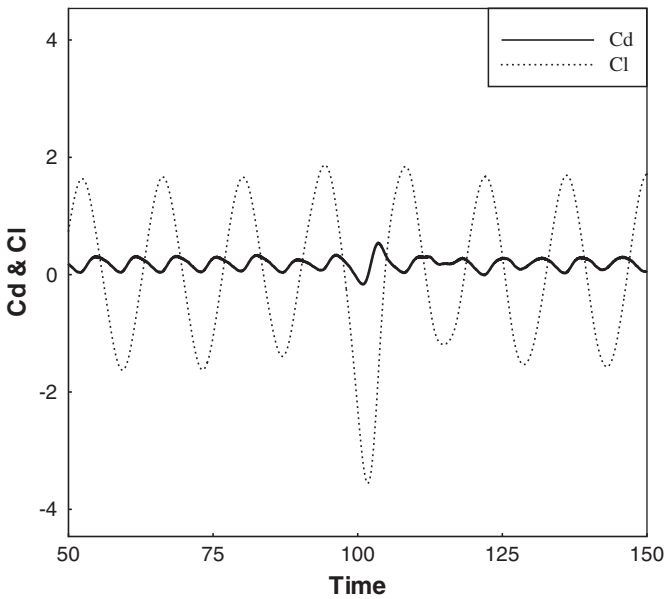

Figure 25. Evolution of the drag and lift coefficients of the upper fish-like body.

moving with respect to each other, and flow around a hovering wing. Numerical simulations were conducted on an elastic filament flapping in the wake of a cylinder and fish-like bodies swimming in quiescent fluid. The results demonstrate the versatility of the present numerical model and show it as an alternative approach for the simulation of fluid–structure interactions.

ACKNOWLEDGEMENTS

The authors are grateful to Professor Charles S. Peskin, Professor Feng Zhi-Gang and Dr Shi Xing for useful discussions during this work. The authors thank the reviewers for their helpful comments and suggestions.

REFERENCES

1. Hirt CW, Amsden AA, Cook JL. An arbitrary Lagrangian–Eulerian computing method for all flow speeds. *Journal of Computational Physics* 1974; **14**:227–253.
2. Liu H, Kawachi K. A numerical study of undulatory swimming. *Journal of Computational Physics* 1999; **155**:223–247.
3. Ramamurti R, Sandberg WC. A three-dimensional computational study of the aerodynamic mechanisms of insect flight. *Journal of Experimental Biology* 2002; **205**:1507–1518.
4. Peskin CS. Numerical analysis of blood flow in the heart. *Journal of Computational Physics* 1977; **25**:220–252.
5. Peskin CS. The immersed boundary method. *Acta Numerica* 2002; **11**:479–517.
6. Goldstein D, Handler R, Sirovich L. Modeling a no-slip flow boundary with an external force field. *Journal of Computational Physics* 1993; **105**:354–366.
7. Saiki EM, Biringen S. Numerical simulation of a cylinder in uniform flow: application of a virtual boundary method. *Journal of Computational Physics* 1996; **123**:450–465.
8. Mohd-Yusof J. Combined immersed-boundary/B-spline methods for simulations of flow in complex geometries. *Annual Research Briefs*, Center for Turbulence Research, NASA Ames and Stanford University, 1997; 317–327.

DOI: 10.1002/fld

9. Fadlun EA, Verzicco R, Orlandi P, Mohd-Yusof J. Combined immersed-boundary finite-difference methods for three-dimensional complex flow simulations. *Journal of Computational Physics* 2000; **161**:35–60.
10. Chen S, Doolen GD. Lattice Boltzmann method for fluid flows. *Annual Review of Fluid Mechanics* 1998; **30**:329–364.
11. Yu D, Mei R, Luo L, Shyy W. Viscous flow computations with the method of lattice Boltzmann equation. *Progress in Aerospace Sciences* 2003; **39**:329–367.
12. Ladd AJC. Numerical simulations of particulate suspensions via a discretized Boltzmann equation. Part I. Theoretical foundation. *Journal of Fluid Mechanics* 1994; **271**:285–310.
13. Ladd AJC. Numerical simulations of particulate suspensions via a discretized Boltzmann equation. Part II. Numerical results. *Journal of Fluid Mechanics* 1994; **271**:311–339.
14. Feng ZG, Michaelides EE. The immersed boundary–lattice Boltzmann method for solving fluid–particles interaction problems. *Journal of Computational Physics* 2004; **195**:602–628.
15. Feng ZG, Michaelides EE. Proteus: a direct forcing method in the simulations of particulate flows. *Journal of Computational Physics* 2005; **202**:20–51.
16. Filippova O, Hänel D. Grid refinement for lattice–BGK models. *Journal of Computational Physics* 1998; **147**:219–228.
17. Yu D, Mei R, Shyy W. A multi-block lattice Boltzmann method for viscous fluid flows. *International Journal for Numerical Methods in Fluids* 2002; **39**:99–120.
18. Bhatnagar PL, Gross EP, Krook M. A model for collision processes in gases. I. Small amplitude processes in charged and neutral one-component systems. *Physical Review* 1954; **94**:511–525.
19. Guo ZL, Zheng CG, Shi BC. Discrete lattice effects on the forcing term in the lattice Boltzmann method. *Physical Review E* 2002; **65**:(046308):1–6.
20. Lai M-C, Peskin CS. An immersed boundary method with formal second-order accuracy and reduced numerical viscosity. *Journal of Computational Physics* 2000; **160**:705–719.
21. Russell D, Wang ZJ. A Cartesian grid method for modeling multiple moving objects in 2D incompressible viscous flow. *Journal of Computational Physics* 2003; **191**:177–205.
22. Xu S, Wang ZJ. An immersed interface method for simulating the interaction of a fluid with moving boundaries. *Journal of Computational Physics* 2006; **216**:454–493.
23. Guo ZL, Zheng CG, Shi BC. Non-equilibrium extrapolation method for velocity and pressure boundary conditions in the lattice Boltzmann method. *Chinese Physics* 2002; **11**:366–374.
24. Wang ZJ. Two dimensional mechanism for insect hovering. *Physical Review Letters* 2000; **85**:2216–2219.
25. Shi X, Phan-Thien N. Distributed Lagrangian multiplier/fictitious domain method in the framework of lattice Boltzmann method for fluid–structure interactions. *Journal of Computational Physics* 2005; **206**:81–94.
26. Zhang J, Childress S, Libchaber A, Shelly M. Flexible filaments in a flowing soap film as a model for one-dimensional flags in a two-dimensional wind. *Nature* 2000; **408**:835–839.
27. Gilmanov A, Sotiropoulos F. A hybrid Cartesian/immersed boundary method for simulating flows with 3D, geometrically complex, moving bodies. *Journal of Computational Physics* 2005; **207**:457–492.
28. Dong GJ, Lu XY. Numerical analysis on the propulsive performance and vortex shedding of fish-like traveling wavy plate. *International Journal for Numerical Methods in Fluids* 2005; **48**:1351–1373.
29. Chew YT, Shu C, Niu XD. Simulation of unsteady and incompressible flows by using Taylor series expansion and least square-based lattice Boltzmann method. *International Journal of Modern Physics C* 2002; **13**:719–738.

DOI: 10.1002/fld